Tomographic Particle Image Velocimetry Study of Stall-delay on the Blade of a 5kW Horizontal-axis Wind Turbine

Hsiao Mun Lee and Yanhua Wu

School of Mechanical & Aerospace Engineering
Nanyang Technological University, Singapore 639798.

Abstract

Tomographic Particle Image Velocimetry (TPIV) and static pressure measurements were performed in a wind tunnel on a scaled model of the rotor blade of a 5kW horizontal-axis wind turbine (HAWT) designed using the Blade Element Momentum (BEM) method. This study is to investigate the physics of the stall-delay phenomenon observed for a rotating blade. TPIV experiments are conducted at several span-wise locations of the blade. The separated flow from the rotating blade are studied and compared with the case of the static stall at similar angles of attack (AOA) and Reynolds number (Re).

Introduction

Flow fields generated by horizontal axis wind turbine (HAWT) are highly complex due to simultaneous presence and interaction of three-dimensional (3D) unsteady flow separation and blade rotational effect. Significant differences were found to exist between two-dimensional (2D) airfoil flow and 3D flow on a rotating blade, particularly for the part of the blade closer to the rotor. The angle of attack at which stall occurs for a rotating blade was found to be larger than for a static blade. This behavior is referred to as the stall delay phenomenon (For example, see Yu et al. 2011). Detailed understanding of stall behavior is required for accurate prediction of peak rotor power in wind energy harnessing practice. Wind turbine's fatigue life may be shortened and the designed generator may be damaged if the turbine's peak performance is under-predicted. Unfortunately, the fundamental physics of the stall delay phenomenon are still elusive.

Some studies in the past have been conducted to understand stall delay. Wood (1991) used the panel method to calculate pressure distributions on a rotating blade and concluded that local solidity was the major parameter on stall delay. Barnsley and Wellicome (1991) identified stall delay by measuring near rotor velocity of a model wind turbine. They used velocity measurements to quantify local incidence and results illustrate the development of enhanced lift incidence due to a delay in the loss of leading edge suction peaks compared to 2D behavior. Numerical simulations (by solving quasi-3D Navier-Stokes equations) have shown that rotating blades produce beneficial vortex structures which are responsible for these moment and force amplifications (Shen an Sorensen 1999).

It is of great interest to measure the instantaneous three-dimensional velocity field in the volume of the flow on the rotating blade to reveal the complex topology of separated flow structures associated with stall delay. The advent of PIV and its developments such as stero-PIV by Arroyo and Greated (1991), multiple planes stereo-PIV by Schroder and Kompenhans (2004) and tomographic PIV by Elsinga et al. (2006) showed the capability of the PIV technique to quantitatively visualize complex flows. However, up to date, no detailed flow measurements using the above advanced velocimetry are performed on rotating turbine blades for the study of stall delay.

Therefore, in the present paper, a study on the stall-delay phenomenon for a down-scaled 5kW upwind horizontal-axis wind turbine designed using Blade Element Momentum method was carried out using tomographic PIV (TPIV) which can yield all three velocity components within a whole fluid volume. The effects of rotation on the stalled blade were investigated using TPIV and the results were compared with those of a statically stalled airfoil at similar AOA. The study of post-stall aerodynamics is conducted using the blade pressure measurement at different span-wise positions of the blade.

Experiments

One of the down-scaled wind turbine rotor blade which is 0.309m in radius was mounted at the vertical center of the test section whose side walls are made of glass and the top and bottom walls are made of acrylic for optical access. It is reasonable to neglect the effect of tower for an upwind turbine, as pointed out by Bak et al. (1999), because the blade of an upwind wind turbine is placed in front of the tower and the tower only produces turbulent wake behind it when wind passes through. Therefore, the tower has no effect on the flow structure of the blade. The blade was tapered and twisted about 25° at the root region. The airfoil is S805 which was designed by National Renewable Energy Laboratory (NREL) for the purpose of HAWT (Somers 1997). The blade was painted with Rhodamine B in order to reduce laser light reflection from the blade surface. The configuration is tested for a free-stream velocity of 1.62m/s with rotational speed of 2.5Hz, yielding a tip speed ratio (TSR) of 3 and Re≈5000 based on the freestream velocity and the chord length at the middle section of the blade.

Tomographic PIV measurements

In tomographic PIV, the three-dimensional locations of the seeding particles in the illuminated fluid volume are reconstructed from the simultaneous recordings of particle images taken from several viewing directions. The measurement technique returns the instantaneous velocity field within the measurement volume by means of 3D particle pattern cross-correlation. Figure 1 shows the schematic of the experimental setup for the current TPIV measurement. A 8mm thick light volume produced by a pair of high-energy (~450mJ/pulse) Nd:YAG lasers is used to illuminated the flow at the suction side of the blade at three spanwise locations, $0.25R$, $0.55R$ and $0.75R$ from the root, where R is the spanwise length of the blade. The seeding particles with a nominal diameter of 1 µm are provided by a Laskin nozzle and are recorded by four 16-bit CCD cameras with 105mm lenses. Each camera's CCD chip has 2456×2058 pixels and the pixel size is 3.45 µm. The cameras are configured in such a way that the backward-scattering of the laser light from the particles are captured yielding similar particle intensities in

the four recordings. For measurements on the rotating blade, the firing of the laser is phase-locked, through the usage of an optical sensor, to the horizontal position of the blade when the blade is rotating upward. 200 TPIV recordings are obtained for measurement at each spanwise location.
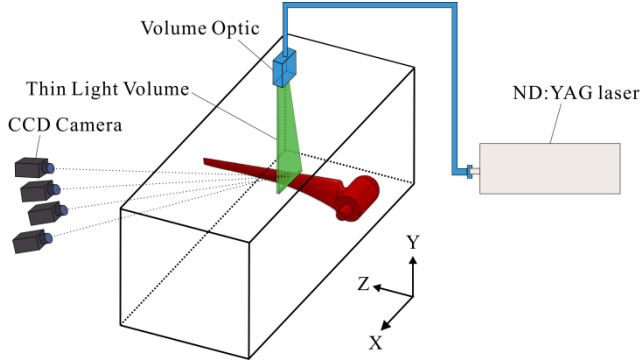
Figure 1. Experimental set-up of TPIV measurements

The FastMART algorithm implemented in LaVision Davis 8.1.1 was used to reconstruct the three-dimensional light intensity field of the particles. A total of 7 iterations of the algorithm were performed. The volume self-calibration as described in Wieneke (2008) was also implemented in Davis to correct the calibration function whose error was shown [10] to be reduced from a typical value of 0.1 voxel to 0.05 vorxel. 3D velocity vector fields were computed by using recursive volumetric cross-correlation of reconstructed particle distributions with the final interrogation volume size of 96×96×96 voxels with 75% overlap. Each resulting velocity field has about 106×92×11 (*x*×*y*×*z*) vectors with a vector grid spacing of 0.76mm, yielding a field of view of about 80mm×70mm×8mm. The velocity fields were validated using a modified median filter to remove erroneous vectors. On average, only about 1~2% bad velocity vectors were removed in any given field and then filled through interpolation. Finally, each vector field was low-pass filtered to remove noise associated with frequencies higher than the sampling frequency of the interrogation. Data processing was performed on a workstation with two quad-core Intel Xeon processors at 2.8Ghz and 128GB memory. It typically took one hour to obtain one volumetric three-dimensional velocity field.

Results and Discussion

Static Pressures

Figure 2 shows the comparison of suction surface pressure coefficients $-C_p = (p - p_\infty)/(0.5\rho U_{ref}^2)$ for similar AOA's between the static and rotating blades at a global TSR of 3 for three span-wise locations, 0.25*R*, 0.55*R* and 0.75*R*. U_{ref} is the relative velocity which was obtained by vectorial summation of upcoming freestream velocity and the rotational velocity at the corresponding central spanwise location, i.e. $U_{ref} = \sqrt{U_\infty^2 + (\Omega r)^2}$. At the 25% of span-wise location, the AOA is 30º. The 2D airfoil data are flat across the entire suction surface of the airfoil, indicating stall with flow separation. In contrast, $-C_p$ of the rotating blade at this location clearly shows significant high values across the chord of the blade. Due to the limited size of the blade, the high leading-edge suction pressure peak that possibly exists before *x/c*=0.1 cannot be measured. The pressure recovery slope obtained in the current study at 0.25*R* is shown in figure 2 (a) to be quite uniform but much more gradual than at the other two spanwise locations. The smaller pressure recovery slope at 0.25*R* of the rotating blade indicates lower adverse pressure gradient at this section.
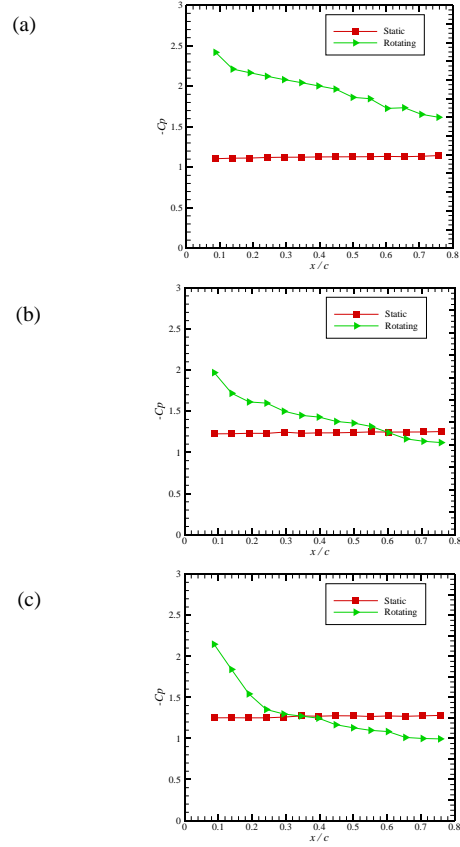
Figure 2. Comparison of C_p for static airfoil and rotating blade at different span-wise locations. (a) 0.25*R* (b) 0.55*R* (c) 0.75*R*

The situation at the 55% of span-wise location (AOA=25º) is similar to that at 0.25*R*. The static pressure indicates that the section has stalled as shown in Figure 2 (b) while the rotating pressure shows apparently higher $-C_p$ before the mid-section of the blade. However, compared with the case at 0.25*R*, the maximum $-C_p$ value at 0.55*R* appears to be smaller as can be indicated by the values at *x/c*=0.1. In addition, at this spanwise location, the $-C_p$ on the upper surface of the rotating blade starts to be lower than that of the static airfoil from *x/c*=0.6. At 0.75*R*, figure 2 (c) shows that the value of $-C_p$ is slightly lower than that at 0.25*R* but higher than at 0.55*R*. The location where $-C_p$ is lower than the static airfoil is found to move closer to the leading edge of the blade at about *x/c*=0.3. The pressure measurements shown in figure 2 are consistent with other studies and with the characteristics of stall delay observed on rotating blades.

The lower suction pressures (corresponding to a higher value of $-C_p$) on the rotating blade were used to explain the increase in lift coefficients in the literature. However, there is still no consistent description of the fundamental physics in fluid mechanics that causes the stall delay phenomenon. Hu *et al.* (2006) concluded that the stall could be delayed by the chord-wise pressure gradient produced by Coriolis forces at the root region of blade. Chaviarropoulos and Hansen (2000) found that the rotating effects were to suppress vortex shedding and the development of the separation bubbles at the trailing edge of the blade. Mean velocity fields measured by TPIV are shown below to provide some insights on the physical process of the stall delay.

Mean velocity fields

Figure 3 show the ensemble averaged velocity field over the static airfoil when AOA=30º. The large-scale flow separation can be observed over the entire suction surface of the airfoil, resulting

in the formation of a very large recirculation bubble near the trailing edge of the airfoil, which is consistent with the flow fields known for a stall with large AOA.
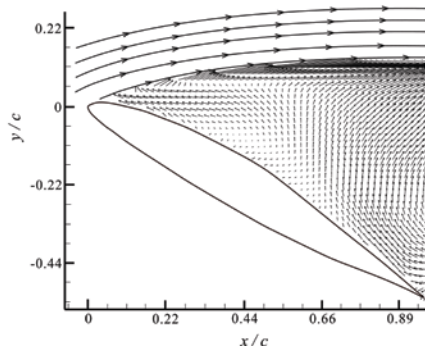
Figure 3. Ensemble averaged velocity field over the static airfoil when AOA=30º. The flow direction is from left to right.

The mean relative velocity fields on the rotating blade at 0.25R, 0.55R and 0.75R are shown in Figure 4. The black vectors show the velocity fields in the back x-y plane of the 8-mm thick fluid volume. It is observed that the flow fields in the x-y planes across the spanwise length within the measured volume are of little difference. The colourful vectors in each plot illustrate the velocities in the streamwise-spanwise (x-z) plane at about y/c= -1. The colors present the magnitudes of the spanwise velocity component, w. It can be observed that w is zero in the freestream region while definitely positive in the separated region in all three measured spanwise locations indicating an outward flow from the blade root to the blade tip. The spanwise flow is also found to be stronger at the outer-board section of the blade.

Comparing Figure 3 with 4 (a), it is seen that there are flow pattern discrepancies between the static airfoil and rotating blade (0.25R) at similar Re and AOA. It can be observed from Figure 4 (a) that the flow separates from the leading edge of the rotating blade. Thereafter, the separated shear layer aches over toward the blade. However, a massive recirculating flow formed over most of suction surface of static airfoil as seen in figure 3 is not observed for the rotating blade. The lack of the recirculation bubble for the rotating blade has also been observed in other numerical studies and the existence of the attached flow has been explained as the reason of the high suction pressures on the suction surface of the rotating blade.

Figure 4 (b) shows that at 0.55R (AOA=25°) of the rotating blade the flow above the suction surface is still attached at this relatively large AOA. In this paper, the flow is called "attached" when the flow near the suction surface of the blade does not illustrate flow reversion but not necessarily mean there is no flow separation. It is seen from figure 4 that the incoming freestream flows at all three spanwise locations are separated from the blade's leading edge forming a detached shear layer. However, the reverse flow is not observed for the rotating blade, different from the separated flow for the static airfoil. Nevertheless, the velocity within the separated flow region above the blade's suction surface appears to be stronger at 0.55R than that at 0.25R.

At the 0.75R (AOA=21°), the flow condition is similar to that of 0.55R. The flow was found to be attached and no flow reversion was found on the blade surface as shown in Figure 4 (c). However, a vortex can be observed near the trailing edge of the blade. The distance between the vortex and the blade surface is about 0.5c. It can be observed that this vortex induces a downward flow toward the suction surface of the rotating blade, which may explain why $-C_p$ near the trailing edge of the blade at

0.75R are significantly decreased to even lower than that on the static airfoil as shown in figure 2 (c).

(c)
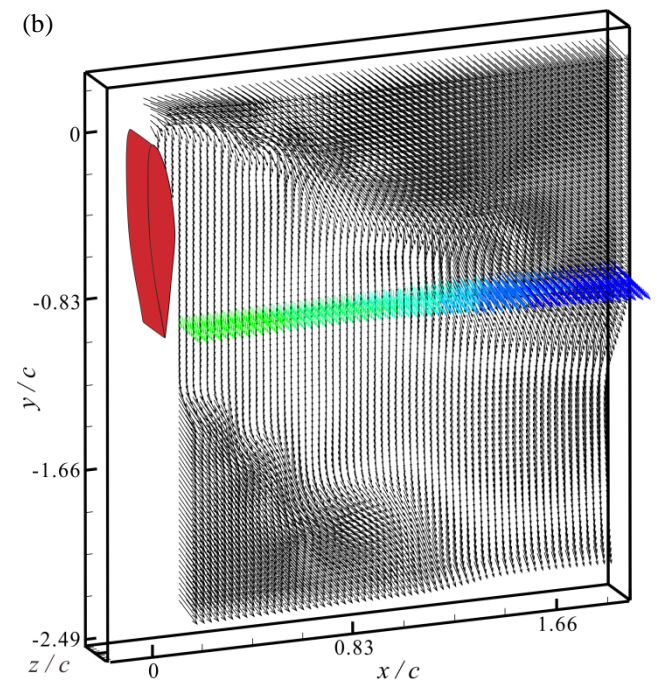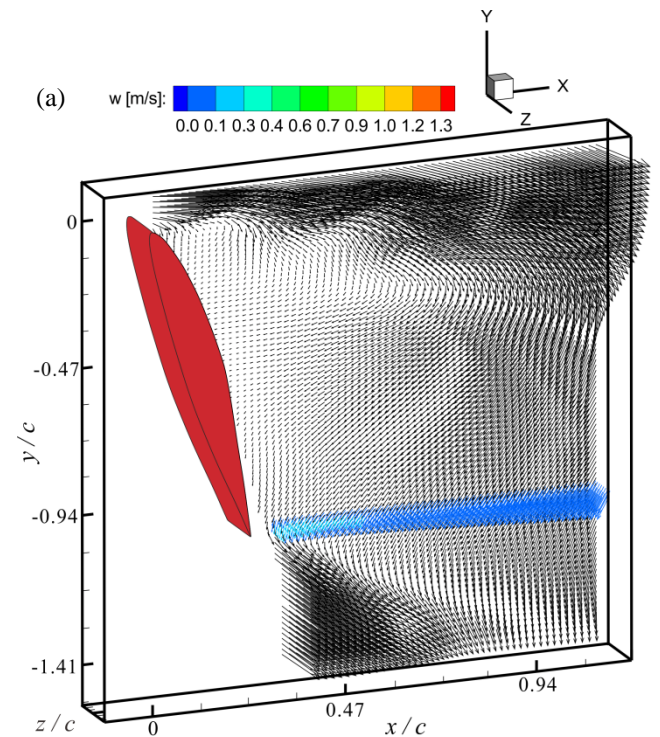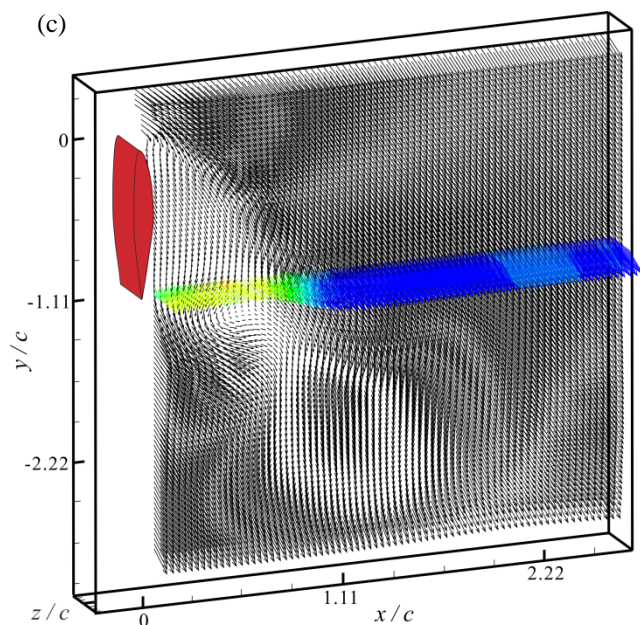
Figure 4. Mean velocity fields over the rotating blade at different span-wise locations (a) 0.25R (b) 0.55R (c) 0.75R.

Summary and conclusions

Surface pressure and tomographic PIV measurements were performed on a rotating down-scaled horizontal-axis wind turbine blade. Results are compared and contrasted with baseline data acquired on a static airfoil under similar angles of attack. This allowed rotational modifications to blade aerodynamics to be characterized in detail. Using these results, some conclusions were drawn. Rotational influences delay stall and augment blade aerodynamic forces. For the static airfoil, chord-wise surface pressure distributions at stall are generally constant. In contrast, the rotating blade exhibits non-constant pressure distributions along the blade chord. At inboard sections, the blade obtains higher values of $-C_p$ or lower static pressures on the suction surface. At outboard sections, pressure gradient is much steeper.

Chord-wise pressure distribution augmentation is strongly linked with the development of attached flow pattern on the blade. At 0.25R with AOA of about 30°, the massive recirculation bubble does not exist for the rotating blade. There is definitely positive however weak spanwise flow toward the blade tip. The incoming flow is observed separated from the leading edge of the blade forming a shear layer. At 0.55 and 0.75r, the flow was found to be attached and no flow reversion was found on the blade surface. The vortex near the trailing edge of the blade at 0.75r might cause a reduction of $-C_p$ or higher static pressures locally. These experiments and analyses have provided detailed characterization of rotational augmentation to HAWT blade aerodynamics. The present and subsequent studies will provide valuable information for understanding the fundamental physics behind the stall delay phenomenon.

References

[1] Arroyo, M. and Greted, C., Stereoscopic Particle Image Velocimetry, Measurement Science and Technology, Vol. 2, 1991, pp 1181-1186.

[2] Bak, C., Fuglang, P., Sorensen, N. N. and Madsen, H. A., Airfoil Characteristics for Wind Turbine, Riso National Laboratory, 1999, Roskilde.

[3] Barnsley, M. J. and Wellicome, J. F., Wind Tunnel Investigation of Stall Aerodynamics for a 1.0m Horizontal Axis Rotor, Journal of Wind Engineering and Industrial Aerodynamics, Vol. 39, 1992, pp 11-21.

[4] Chaviarropoulos, P. K. and Hansen, M. O. L., Investigating Three-Dimensional and Rotational Effects on Wind Turbine Blades by Means of a Quasi-3D Navier-Stokes Solver, Journal of Fluids Engineering, 2000, Vol. 122, pp 330.

[5] Elsinga, G. E., Scarano, F., Wieneke, B. and van Oudheusden, B . W., Tomographic Particle Image Velocimetry, Experiments in Fluids, Vol. 41, 2006, pp 933-947.

[6] Hu, D., Hua, O. and Du, Z., A Study on Stall-Delay for Horizontal Axis Wind Turbine, Renewable Energy, Vol. 31, 2006, pp 821-836.

[7] Schroder, A. and Kompenhans, J., Investigation of a Turbulent Spot Using Multi-Plane Stero Particle Image Velocimetry, Experiments in Fluids, Vol. 36, pp 82-90.

[8] Shen, W. Z. and Sorensen, J. N., Quasi-3D Navier-Stokes Model for a Rotating Airfoil, Journal of Computational Physics, Vol. 150, 1999, pp 518-548.

[9] Somers, D. M., Design and Experimental Results for the S805 Airfoil, National Renewable Energy Laboratory, 1997.

[10] Wieneke, B., Volume Self-Calibration for 3D Particle Image Velocimetry, Experiments in Fluids, Vol. 45, 2008, pp 549-556.

[11] Wood, D. H., A Three-Dimensional Analysis of Stall-delay on a Horizontal Axis Wind Turbine, Journal of Wind Engineering and Industrial Aerodynamics, Vol. 37, 1991, pp 1-14.

[12] Yu, G., Shen, X., Zhu, X. and Du, Z., An Insight into the Separate Flow and Stall Delay for HAWT, Renewable Energy, Vol. 26, 2011, pp 69-7